Comparison of Cellular Architecture, Axonal Growth, and Blood Vessel Formation Through Cell-Loaded Polymer Scaffolds in the Transected Rat Spinal Cord

Nicolas N. Madigan, MD, PhD,[1,2] Bingkun K. Chen, MD, PhD,[1] Andrew M. Knight, PhD,[1]
Gemma E. Rooney, PhD,[1] Eva Sweeney,[2] Lisa Kinnavane,[2]
Michael J. Yaszemski, MD, PhD,[3] Peter Dockery, PhD,[2] Timothy O'Brien, MD, PhD,[2]
Siobhan S. McMahon, PhD,[2] and Anthony J. Windebank, MD[1]

The use of multichannel polymer scaffolds in a complete spinal cord transection injury serves as a deconstructed model that allows for control of individual variables and direct observation of their effects on regeneration. In this study, scaffolds fabricated from positively charged oligo[poly(ethylene glycol)fumarate] (OPF^{+}) hydrogel were implanted into rat spinal cords following T9 complete transection. OPF^{+} scaffold channels were loaded with either syngeneic Schwann cells or mesenchymal stem cells derived from enhanced green fluorescent protein transgenic rats (eGFP-MSCs). Control scaffolds contained extracellular matrix only. The capacity of each scaffold type to influence the architecture of regenerated tissue after 4 weeks was examined by detailed immunohistochemistry and stereology. Astrocytosis was observed in a circumferential peripheral channel compartment. A structurally separate channel core contained scattered astrocytes, eGFP-MSCs, blood vessels, and regenerating axons. Cells double-staining with glial fibrillary acid protein (GFAP) and S-100 antibodies populated each scaffold type, demonstrating migration of an immature cell phenotype into the scaffold from the animal. eGFP-MSCs were distributed in close association with blood vessels. Axon regeneration was augmented by Schwann cell implantation, while eGFP-MSCs did not support axon growth. Methods of unbiased stereology provided physiologic estimates of blood vessel volume, length and surface area, mean vessel diameter, and cross-sectional area in each scaffold type. Schwann cell scaffolds had high numbers of small, densely packed vessels within the channels. eGFP-MSC scaffolds contained fewer, larger vessels. There was a positive linear correlation between axon counts and vessel length density, surface density, and volume fraction. Increased axon number also correlated with decreasing vessel diameter, implicating the importance of blood flow rate. Radial diffusion distances in vessels significantly correlated to axon number as a hyperbolic function, showing a need to engineer high numbers of small vessels in parallel to improving axonal densities. In conclusion, Schwann cells and eGFP-MSCs influenced the regenerating microenvironment with lasting effect on axonal and blood vessel growth. OPF^{+} scaffolds in a complete transection model allowed for a detailed comparative, histologic analysis of the cellular architecture in response to each cell type and provided insight into physiologic characteristics that may support axon regeneration.

Introduction

HYDROGEL POLYMER SCAFFOLDS can integrate combinations of therapies necessary for functional spinal cord repair.[1–3] Strategies to both promote axonal growth[4] and reduce inhibitory cues[5] will be necessary to facilitate regeneration of neural tissue through the barriers consequent to spinal cord injury (SCI).[6] Nervous tissue regeneration may be supported by the matrix properties of the selected polymer and the architecture of the scaffold. Permissive microstructures such as pores, grooves, polymer fibers, and surface modifications may provide improved axon adherence and growth directionality.[7] Scaffolds or patterned substrates derived from natural materials such as collagen,[8] hyaluronic acid,[9] agarose,[10] fibrin,[11] fibronectin,[12] and chitosan[13] have been proposed as scaffolds. Synthetic scaffolds include biodegradable hydrogels based on polyethylene glycol (PEG)[14] or nonbiodegradable hydrogels based on methacrylate.[15] We recently compared four different

[1]Department of Neurology, Mayo Clinic College of Medicine, Mayo Clinic, Rochester, Minnesota.
[2]Department of Medicine, Regenerative Medicine Institute (REMEDI), National University of Ireland, Galway, Ireland.
[3]Department of Orthopedic Surgery, Mayo Clinic College of Medicine, Mayo Clinic, Rochester, Minnesota.

polymer types,[16] demonstrating improved axonal density and accuracy of growth orientation using the positively charged hydrogel polymer oligo[poly(ethylene glycol)fumarate] (OPF$^+$). OPF is a PEG-based macromer incorporating a fumarate moiety that is photo-cross-linked to form a soft, porous biodegradable hydrogel.[14] OPF can be polymerized with monomer [2-(methacryloyloxy) ethyl]-trimethylammonium chloride (MAETAC) to produce the positively charged substrate (OPF$^+$). OPF$^+$ surface enhances neuronal cell attachment, Schwann cell migration, and axonal myelination *in vitro*.[17]

Cell implantation within scaffolds remains a foundation for combination therapies, utilizing supportive properties innate to the cell line, and genetic modification[18] to deliver neurotrophic molecules[19] or targeted molecular therapies.[20,21] Schwann cells have been consistently shown to be one of the most effective therapeutic cell types in regeneration after experimental SCI.[22] These cells reduce the size of spinal cysts, remyelinate axons,[23] and improve functional recovery in SCI.[24] Schwann cells have also been shown to produce a number of growth factors that initiate and support the growth of axons, and to express cell adhesion molecules on their surface for axon guidance.[25] Autologous Schwann cells have recently been introduced as a potential therapy in patients with SCI.

Mesenchymal stem cells (MSCs) in SCI have also been shown to enhance axonal regeneration and promote functional recovery in animal models,[26] by means of trophic effects and tissue-sparing immunomodulation.[27] MSCs may provide both a cellular substrate and a source of secreted growth factors.[28] In central nervous system (CNS) healing, MSCs have been shown to secrete vascular endothelial growth factor, nerve growth factor, and brain-derived neurotrophic factor.[29] They increase angiogenesis, and stimulate regeneration via glial-axonal remodeling.[30] Neurogenesis and synaptogenesis may occur from resident neural stem cells[31] that are stimulated by factors secreted by implanted MSCs. MSCs may also supply secreted signals for the inhibition of scar formation and apoptosis.[32] MSC trophism is likely to be of greater significance for CNS tissue repair than differentiation of the cell toward nervous system phenotypes *in situ*.[33] For example, neurally differentiated MSCs lose their neuronal phenotype upon implantation.[34] We similarly have proposed that MSCs do not differentiate into neurons or neural support cells upon direct implantation into the spinal cord.[35]

We have recently published controlled analyses of factors influencing axonal regeneration through multichannel scaffolds, including the cell type (Schwann cells compared with neural stem cells[36]), and scaffold channel size.[37] Schwann cells performed better than MSCs in supporting axonal growth when implanted in OPF$^+$ scaffolds.[38] This difference appeared to be related to blood vessel formation within the channels of the scaffolds. In that study, there were less capillaries but more axons in Schwann cell-loaded scaffolds compared with those containing MSCs. Treatment with cyclic-AMP was associated with an increase in axonal number and a decrease in capillary number.[38]

In the present study, multichannel OPF$^+$ scaffolds were loaded with either Schwann cells or MSCs from the bone marrow of transgenic rats with expression of the enhanced green fluorescent protein (eGFP-MSCs). The cellular composition of the scaffold channels and a detailed stereological analysis of neovascular morphology suggest a strong relationship between vessel size, number, and distribution and axonal regeneration.

Materials and Methods

Cell isolation and characterization

Rat MSC primary cultures were obtained from femur and tibia bone marrow, as previously described[39] from wild-type (wt) and eGFP-transgenic Sprague Dawley (SD) animals (CZ-004 [SD TgN(act-EGFP) OsbCZ-004], Genome Information Research Center, Osaka University, Japan, $n = 18$). The capacity for eGFP-MSC cultures to differentiate into adipocyte, osteocyte, and chondrocyte lineages was assessed as we have previously described.[39] Rat Schwann cells were cultured from the sciatic nerves of 2–5 day old newborn pups as we have described.[16,36]

Flow cytometry analysis

eGFP-MSCs were characterized as previously described.[38,43] Cells were fixed in phosphate-buffered saline (PBS) with 4% paraformaldehyde and incubated with primary antibodies to CD90, CD11b/c (mouse anti-rat, 1:200) (Biolegend), CD73 (ecto 5′ nucleosidase) (mouse anti-rat, 1:100), CD45 (mouse anti-rat, 1:200), CD71 (Ox-26) (mouse anti-rat, 1:100), and CD172 (Ox-41; signal regulatory protein [SIRP]) (mouse anti-rat, 1:100; BD Biosciences). Goat-anti mouse IgG (H+L) secondary antibody conjugated to Alexa-Fluor® 647–R-phycoerythrin (PE) (Invitrogen) was used at a dilution of 1:100. FACS analysis for eGFP and PE signal was performed on 50,000 events using FACS Calibur apparatus (Becton-Dickinson). Controls included cells only, cells with secondary antibody only, isotype control, and eGFP-positive and negative fluorescent controls.

OPF$^+$ scaffold fabrication

OPF macromer was synthesized as a condensation reaction between PEG and triethyamine and dissolved in deionized water containing 0.05% (w/w) of photoinitiator (Irgacure 2959; Ciba-Specialty Chemicals) and 0.3 g of the cross-linking reagent N-vinyl pyrrolidinone. OPF was chemically modified at 20% w/w with the positively charged monomer MAETAC (80% wt in water; Sigma-Aldrich).[17] MAETAC is a bifunctional molecule containing both a pH-independent cationic head (quaternary ammonium) and a reactive methacryloyl group that copolymerizes with the fumarate group of the OPF. OPF$^+$ hydrogel scaffolds were fabricated[16] by mold injection of liquid polymer, cast over seven parallel wires of 290 μm diameter and polymerized by exposure to UV light (365 nm) at an intensity of 8 mW/cm^2 (Black-Ray Model 100AP). Individual scaffolds were cut into 2 mm lengths and sterilized prior to cell loading by immersion in serial dilutions of ethanol.

OPF$^+$ scaffold cell loading and surgical implantation

eGFP-MSC or Schwann cell cultures were resuspended in undiluted Matrigel™ (BD Biosciences) at a density of 50,000 cells/μL and loaded to 238,000 cells per scaffold (34,000 cells per channel). Scaffolds were loaded with Matrigel alone in control animals. All surgical and care procedures involving animals were approved by the Institutional

Animal Care and Use Committee (IACUC) at the Mayo Clinic, Rochester, MN, in accordance with the National Institutes of Health, and the Institute for Laboratory Animal Research (ILAR) within the National Academy of Sciences.[40] Surgical materials and full methodology was as we have previously described.[16] Laminectomy through the T8-T10 level, T9 transection, and scaffold implantation was performed on female SD rats weighing 230–250 g (Harlan Laboratories). Hindlimb locomotor function was assessed in open field testing by three independent observers blinded to the animal group at intervals of 2 and 4 weeks after surgery. Each animal's movement was observed in an open plastic box for 5 min, with record taken of individual hindlimb ankle, knee and hip joint movement, weight support, toe clearance, tail position, and coordination of paw position placement in gait. Function was scored by means of the established 21 point Basso, Beattie, and Bresnahan (BBB) locomotor rating scale.[41] The BBB score for each animal was calculated by recording the highest movement scores of the two hindlimbs, and presented as the average of the three observations. Animals were sacrificed following deep anesthesia by transcardial perfusion with 4% paraformaldehyde in PBS. The scaffold and surrounding cord was dissected free, fixed, and embedded in paraffin.

Antibodies and immunohistochemistry

Primary antibodies were used against glial fibrillary acid protein (GFAP) (Rabbit anti-rat, 1:100; Dako),[42,43] S-100 antigen (mouse anti-rat, 1:300; Biogenex) and axon neurofilament protein (mouse anti-rat monoclonal antibody, Dako; 1:50). Blood vessels were identified with primary antibody to collagen IV (polyclonal rabbit IgG, 1:300; Abcam).[44] Secondary antibodies included Alexa-Fluor® 546 anti-rabbit IgG (1:100; Invitrogen Molecular Probes) (GFAP); IgG-linked FITC secondary label (1:100; Millipore Chemicon)[45] and Cy-5 linked anti-mouse IgG secondary (1:100; Millipore Chemicon) (S-100 and collagen IV); and anti-mouse IgG biotinylated secondary antibody (1:100; Dako)[46] (Neurofilament).

Rehydrated tissue sections were permeabilized in PBS with 0.4% Triton X-100. Slides were immersed in citrate buffer (10 mM sodium citrate and 0.05% Tween 20, pH 6.0) preheated to 96°C for antigen retrieval. Sections were incubated with primary antibody in a humidified slide chamber overnight at 4°C followed by serial washing (PBS with 0.1% Triton X-100) and application of secondary antibody. Antibody-conjugated Horseradish Peroxidase was bound to Streptavidin (ExtrAvidin-Peroxidase™; Sigma-Aldrich), with 3,3′-diaminobenzidine (DAB) as a tertiary chromogen.

Microscopy

Chromogen-stained channels were observed with a Leica DM1000 Upright Fluorescence Microscope. Fluorescent imaging was acquired with an Olympus IX81 Inverted Structured Light Microscope. Z-Stacked images were compiled from an 8 μm thickness with slices of 0.5 μm using an Optigrid structured light device. An Olympus IX81 Inverted Microscope with a Yokogawa CSU-X1 Spinning Disk Unit was used for eGFP and Cy-5 imaging. Confocal microscopy was done on a Carl Ziess LSM 780 confocal microscope (software version 8.0) at 40× magnification under water immersion.

Image analysis

Acquired images were analyzed using the NIH software, ImageJ (http://rsbweb.nih.gov/ij/download.html). Color channels were split into separate images, converted to grayscale, and an intensity threshold level was set for each stain, which was kept constant. Each image was then converted to a 1 bit black and white image. For area calculations, the length (in pixels) of a graticule division was calibrated into the software, having imaged the graticule on the same microscope and at the same magnification as the image being analyzed. The area of the number of pixels making up the stained area is presented as a proportion of the number of pixels comprising the total channel area. Six scaffolds in each animal group were analyzed at single tissue sections at ¼, ½, and ¾ length intervals through the scaffold. Mean channel cross-sectional area was derived from 94 Matrigel, 55 Schwann cell and 112 eGFP-MSC channels. Mean proportional area occupied by GFAP, S-100, and eGFP-positive cells was derived from analysis of 91 Matrigel, 70 Schwann cell, and 72 eGFP-MSC channels. Statistical analysis was done as a comparison of means with Kruskal–Wallis analysis of variance (ANOVA) and a Dunn's multiple comparison of means posttest.

Axon counting

Axons within the scaffold channels were identified by staining with primary antibody to neurofilament protein using a biotinylated secondary antibody and visualized with DAB chromogen. Axons appeared as discrete dark brown points in cross section within the channel core, and they were counted using 40× and 100× objective lenses in the same manner as we have previously described.[16,36,37] The number of axons seen across all seven channels in a single scaffold section was summated. Individual sections were chosen at ¼, ½, and ¾ length intervals through each scaffold, providing three sample data points per animal in six animals per group, $n = 18$. The Kruskal–Wallis test (nonparametric ANOVA) was used determine significant differences in median axonal counts between the three animal groups.

Stereology for blood vessel quantification

An unbiased stereological approach[47,48] was used to calculate estimates of volume fraction (Vv), length density (Lv), and surface density (Sv) of blood vessels within each channel at quarter length intervals through the scaffold. The total number of channels analyzed was 93 Matrigel, 86 Schwann cell, and 91 eGFP-MSC channels. The volume fraction (Vv) represented the proportion of each unit volume in the reference channel space occupied by a vessel structure. A simple point grid was overlaid onto the channel image field in a random orientation. The number points overlaying a vessel feature was counted as a proportion of the total number of points found to be within the reference space. The volume fraction was calculated as the total sum of feature points divided by the total sum of reference points,

$$Vv(Y, ref) = \frac{\sum_{i=1}^{m} P(Y)i}{\sum_{i=1}^{m} P(ref)i}$$

where Y is the vessel feature, ref is the channel surface, m is the number of fields analysed, and i is the number of point intersections.

The length density (Lv) represented the combined length of vessel structures embedded within a channel section. A counting frame grid was laid over the channel image in a random orientation. The area of the counting frame was associated with a central point, used to measure the reference volume. A vessel was counted if it fell either fully within the framed area or lay partially outside and overlapped with the "acceptance lines" making up the top horizontal and right hand vertical boundary of the frame. Any vessel that overlapped the "forbidden lines" (bottom horizontal and left-hand vertical boundary), or fell outside of the frame area was not counted. The length density was calculated as the ratio of the sum of grid-vessel intersections (i) to the sum of points falling in the reference channel space over a given field number (n),

$$Lv(Y, ref) = 2 \bullet \frac{\sum_{i=1}^{n} Q_i}{a/f \bullet \sum_{i=1}^{n} P_i}$$

where Q is the number of vessel profiles correctly sampled by the frame, P is the number of frame-associated points, and a/f is the area of the frame at the final magnification ($3600 \, \mu m^2$).

The surface density (Sv) of the vessels represented the surface area of blood vessel features per volume of the reference space. A series of linear test probes associated with a reference point was used. The Sv was calculated as twice the sum of number the line-vessel intersections in inverse proportion to the sum of points striking the channel surface over a given field number (n), when the length of the line associated with the reference point (l/p) is known at the final magnification:

$$Sv(Y, ref) = \frac{2 \bullet \sum_{i=1}^{n} I_i}{l/p \bullet \sum_{i=1}^{n} P_i}$$

Physiologic parameters derived from volume fractions

Anatomical estimates V(Y) for blood vessel volume, length, and surface area in scaffold channel sections were calculated from the volume fraction estimates. The relationship of total volume was determined:

$$V(Y) = V(ref) \bullet Vv(Y, ref)$$

The average channel volume V (ref) was calculated from the mean channel area at the corresponding scaffold quarter interval multiplied the approximate thickness of the tissue section.

Mean vessel diameter, cross-sectional area, and radial diffusion distance were derived from proportions of volume fraction, length density, and surface density.[49] The mean vessel diameter was calculated from the ratio of surface to length density, according to the equation:

$$\overline{d} = \frac{Sv}{Lv\pi}$$

The mean cross-sectional area was calculated from all three stereologic estimates and derived from the diameter calculation, as being

$$\overline{a} = \frac{Vv}{Lv} \frac{\pi d^2}{4}$$

Length density inversely applies to the radial diffusion distance, a robust indication of a cylindrical zone of diffusion around the vessel wall.[49] This parameter was calculated from Lv estimates according to the equation:

$$r(diff) = \frac{1}{\sqrt{\pi \bullet Lv}}$$

Correlations between axon number and vessel stereology estimates

Data pairs (median axon number and volume fraction estimates) were obtained from the same animal, and from the same quarter length through each scaffold, in Matrigel and Schwann cell groups. Statistical correlation was calculated using GraphPad 5 software, assuming a nonparametric correlation yielding Spearman r coefficients and p-values by two-tailed analysis.

Results

OPF⁺ scaffold implantation and regenerated tissue architecture

OPF^{+17} hydrogel scaffolds were fabricated by injection molding and loaded with control Matrigel™, Schwann cells or eGFP-MSCs suspended in Matrigel™ at a density of 50,000 cells per μL (Fig. 1A). The cell population of eGFP-MSC cultures was homogeneously eGFP⁺/CD90⁺, eGFP⁺/CD71⁺, and eGFP⁺/CD172⁺ by surface marker FACS analysis, but heterogeneous for CD73 positivity. No marker expression was seen for leukocyte (CD45) or macrophage (CD11b/c) cell types.

Cell-loaded and control scaffolds were surgically implanted between the rostral and caudal ends of complete spinal cord transections at the level T9 in 10 control, 8 SC and 10 MSC animals. Postoperative animal mortality was 10% for the control group, 25% for the SC group, and 33% for the MSC group, with an overall mortality of 20%. Animals were scored for improvements in hindlimb motor function according to the BBB scoring system, at 2 and 4 weeks postoperatively. Scores were consistent with complete postoperative paraplegia and animals demonstrated no significant functional recovery of motor function. Mean BBB scores at 2 weeks were 3.81 ± 0.82 in Matrigel animals, 4.0 ± 0.96 in Schwann cell, and 4.19 ± 0.70 in MSC animals. Mean BBB scores at 4 weeks were 3.81 ± 0.76 in control, 5.0 ± 0.97 in Schwann cell, and 3.81 ± 0.77 in eGFP-MSC animals.

Animals were sacrificed 4 weeks after scaffold implantation. With the spinal cord dissected free, the scaffolds were seen to be well aligned and fully integrated into transected ends of the cord, with scarring evident at the transition areas (Fig. 1B). Channels of regenerated tissue were seen to extend through the length of the translucent hydrogel, and they were preserved in their orientation following sectioning (Fig. 1C).

The cellular architecture of scaffold channels in each of the animal groups was assessed at quarter length intervals with hematoxylin and eosin staining. All channels were highly cellular and without areas of gross tissue necrosis. An inner
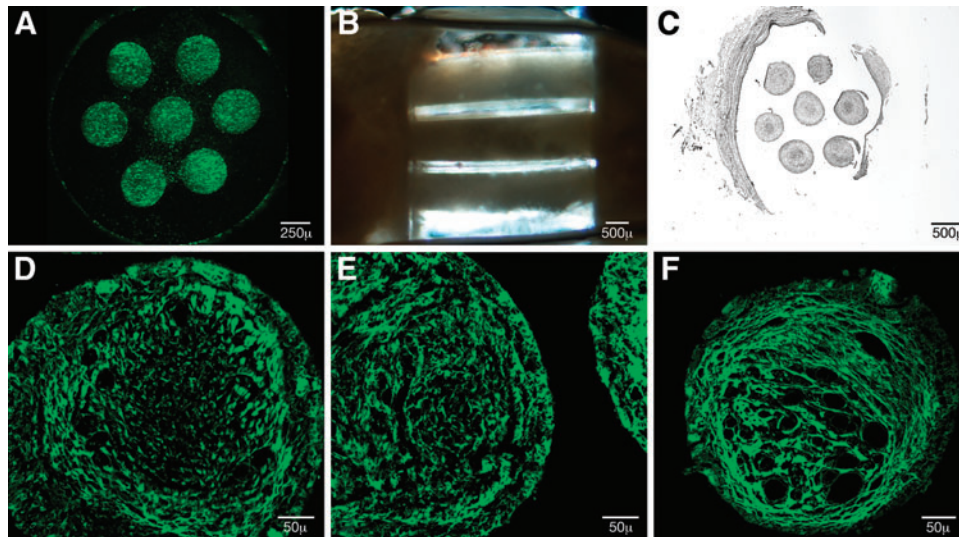
FIG. 1. Positively charged oligo[poly(ethylene glycol)fumarate] (OPF) scaffolds were loaded with Matrigel alone, Schwann cells, or mesenchymal stem cells derived from enhanced green fluorescent protein (eGFP-MSCs) suspended in Matrigel. Cell-loaded scaffolds were surgically implanted into a T9 complete spinal cord transection ($n=10$ animal groups) and were histologically analyzed at quarter length intervals through the scaffold as individual channels. **(A)** Fluorescent eGFP-MSCs densely fill OPF$^+$ scaffold channels following cell loading 238,000 cells per scaffold. **(B)** Implanted polymer scaffolds were aligned and integrated between the transected ends of the spinal cord, conveying cables of tissue growth at 4 weeks within the translucent hydrogel. **(C)** The overall architecture of the scaffold was preserved following tissue sectioning. The mean cross-sectional area for Matrigel channels ($120,990 \pm 1806\,\mu m^2$) ($p<0.001$) and Schwann cell channels ($114,264 \pm 2363\,\mu m^2$) ($p<0.01$) was higher than eGFP-MSC channels ($106,691 \pm 1677\,\mu m^2$) postfixation in 94 Matrigel, 55 Schwann cell, and 112 eGFP-MSC channels analyzed. **(D–F)** Eosin autofluoresence of representative Matrigel, Schwann Cell, and eGFP-MSC channels (left to right) demonstrated structural compartmentalization into peripheral and core areas with delineated transition. Blood vessel structures dominated the core area in eGFP-MSC channels. Multinuclear cellular aggregates were consistently seen at the tissue interface with the polymer. Color images available online at www.liebertpub.com/tea

core tissue type could be histologically distinguished from an outer circumferential layer extending to the channel wall. Using eosin autofluorescence,[50] inner and outer channel compartments were seen to be divided by a ring of brightly fluorescent stranding (Fig. 1D–F). Multinuclear cells were seen at the channel interfaces with the polymer. In the Schwann cell channel (Fig. 1E), the demarcation between tissue comprising the core and periphery was abrupt. In the eGFP-MSC channel (Fig. 1F), the distribution of tissue was primarily in relation to the prominent vasculature in the core.

Quantification of the cellular composition in scaffold channel compartments

GFAP-positive cells uniformly lined the inner surface of the polymer channel wall in each animal group. In the channel core, GFAP staining was isolated to individual cells or clusters and often colocalized with S-100 staining (Fig. 2A–C, E). eGFP-MSCs were present at 4 weeks post-implantation at a low percentage compared with the implantation volume. High power imaging verified eGFP-MSC cellularity (Fig. 2D). S-100 and GFAP colocalization was also seen in the core of eGFP-MSC channels (Fig. 2E).

The proportional area occupied by S-100, GFAP-positive, and eGFP cells in a given channel was calculated using ImageJ analysis software (Fig. 3A). A significantly higher percentage of GFAP staining was measured within Matrigel-filled channels ($30.19\% \pm 1.5\%$) ($n=91$ channels) when compared with eGFP-MSC ($19.15\% \pm 2.5\%$) ($n=72$ chan-

nels) and SC-filled channels ($17.10\% \pm 1.28\%$), $p<0.0001$ ($n=70$ channels). There were no significant differences between Matrigel ($5.32\% \pm 0.37\%$), Schwann cell ($7.31\% \pm 0.77\%$), and eGFP-MSC ($10.07\% \pm 1.03\%$) with regard to the proportion of S-100 positive staining. Surviving MSCs comprised $9.81\% \pm 0.98\%$ of the channel area.

Quantification of axon numbers showed significantly more axons regenerating in the Schwann cell group (Fig. 3B). The median number of axons counted at each quarter length interval through a scaffold was 270 axons in control animals compared to 1313 in the Schwann cell group ($p<0.01$) and 12 axons in the eGFP-MSC group ($p<0.001$) ($n=18$ scaffold sections).

Axon number and blood vessel fraction correlations

Axons stained with antibody to Neurofilament protein (Fig. 4A–C) and blood vessels identified with antibody to collagen IV (Fig. 4D–F). A higher density of axons was observed in Schwann cell channels (Fig. 4B). Axons and blood vessels were confined to the central channel core. Small caliber, thin-walled blood vessels were seen in Matrigel and Schwann cell channels (Fig. D, E), while larger diameter, thick-walled vessels predominated the core of eGFP-MSC channels. Fluorescent GFP-MSCs could be seen in close proximity to vessel structures, often aligned around the vessel border (Fig. 4F).

An unbiased stereologic approach was taken to estimate the volume fraction (Vv), length density (Lv), and surface density (Sv) of vessel structures. Physiologic estimates for
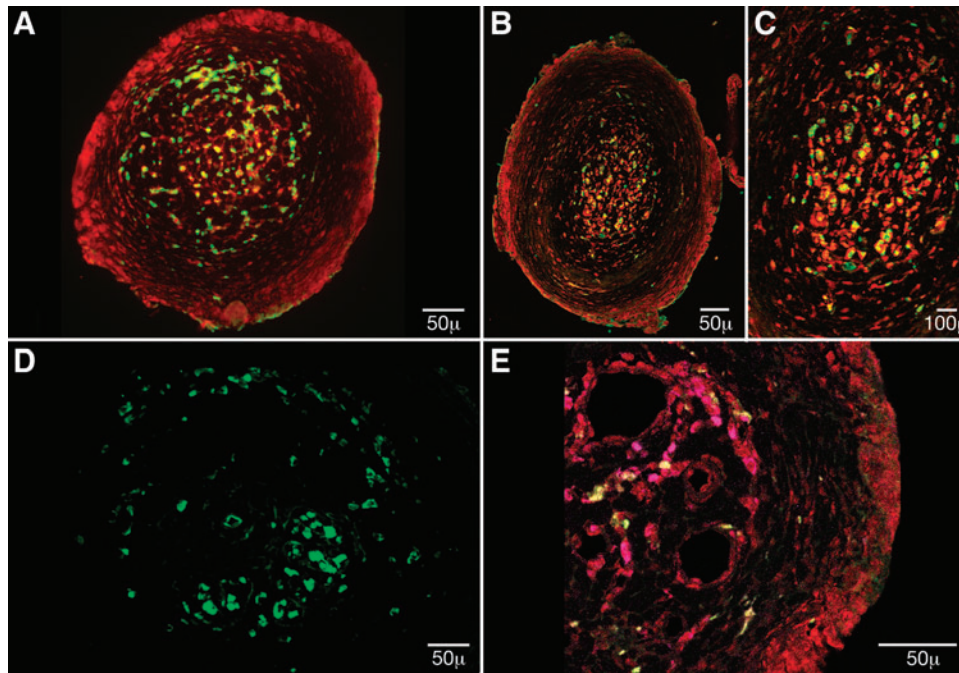
FIG. 2. The cellular composition of scaffold channels was identified with antibodies to glial fibrillary acid protein (GFAP) (red) and the S-100 antigen (green) in **(A)** Matrigel and in **(B)** Schwann cell channels at $20\times$ magnification and **(C)** Schwann cell channels at $60\times$ magnification. GFAP staining uniformly demarcated the channel periphery, while S-100 and GFAP staining colocalized in discrete cell populations within the core region. **(D)** eGFP-MSCs cellularity was further visualized at $40\times$ magnification. **(E)** GFAP (red) peripheral staining, and GFAP/S-100 (magenta) colocalization in the channel core was also a feature of eGFP-MSC (green) channels, seen here at $40\times$ magnification. Color images available online at www.liebertpub.com/tea

each channel section were calculated by correlating the fractional volumes with the tissue section volume. In Matrigel channels, the mean blood vessel volume (V) (Fig. 5A) was $28,770 \pm 2894 \, \mu m^3$, significantly less than both the Schwann cell channel vessel volume ($131,688 \pm 15,399 \, \mu m^3$, $p < 0.01$) and the eGFP-MSC vessel volume ($161,349 \pm 11,898 \, \mu m^3$, $p < 0.001$). No significance difference was seen in vessels volume between the Schwann cell and MSC channel.

The mean total vessel length (L) (Fig. 5B) in Schwann cell channel sections was significantly longer ($1175 \pm 147 \, \mu m$), than Matrigel ($412 \pm 41 \, mm$) ($p < 0.001$) and MSC channels ($564 \pm 44 \, mm$) ($p < 0.001$). The vessel surface areas (S) (Fig. 5C) in Schwann cell ($20,404 \pm 2231 \, \mu m^2$) and MSC ($13,508 \pm 819 \, \mu m^2$) channels both were increased over the vessel surface area in Matrigel ($7875 \pm 662 \, \mu m^2$) channels ($p < 0.001$ and $p < 0.01$ respectively).
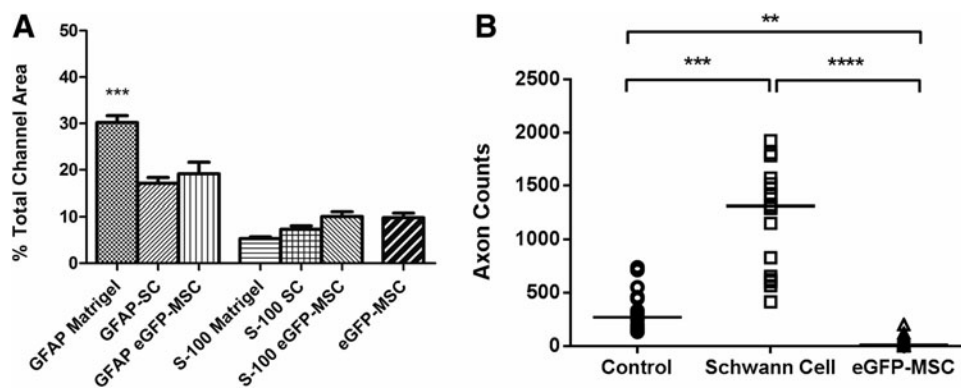

FIG. 3. **(A)** Mean proportional channel area occupied by GFAP, S-100, and eGFP-positive cells in each animal group. A significantly higher proportion of GFAP staining was seen in the Matrigel group ($p < 0.001$) ($n = 91$ channels) than in Schwann cell ($n = 70$ channels) or eGFP-MSC channels ($n = 72$). **(B)** Axon numbers in Matrigel, Schwann cell, and eGFP-MSC scaffolds were calculated as the median value of axons counted in tissue sections spaced at quarter length intervals through the scaffold ($n = 18$ scaffold sections per animal group). Schwann cell scaffolds contained higher axon numbers than were seen in Matrigel scaffolds, while eGFP-MSC-loaded scaffolds did not support axonal growth to any significant extent.
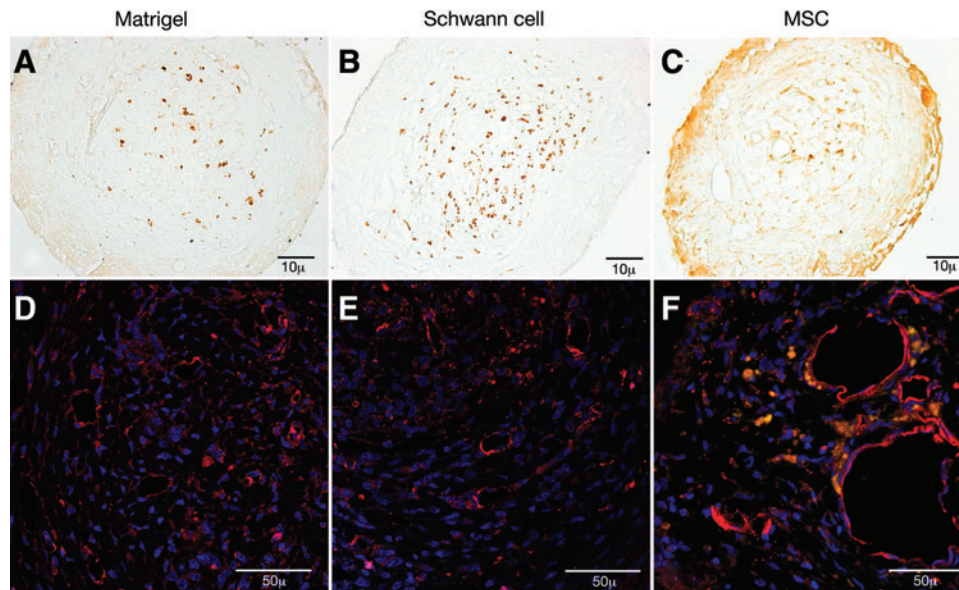
FIG. 4. **(A–C)** Axonal neurofilament protein was visualized with antibody staining and the 3,3′-diaminobenzidine chromogen (brown) in Matrigel, Schwann Cell, and eGFP-MSC channels (10× magnification). **(D–F)** Collagen IV antibody staining (red) identified blood vessels in Matrigel, Schwann cell, and eGFP-MSC (green) channels counterstained with DAPI nuclear staining (blue) (40× magnification). Matrigel and Schwann cell channel blood vessels were of small diameter and were thin walled. Blood vessels in eGFP-MSC channels were of larger diameter. eGFP-MSCs were frequently seen to be aligned along the vessel perimeter **(F)**. Color images available online at www.liebertpub.com/tea
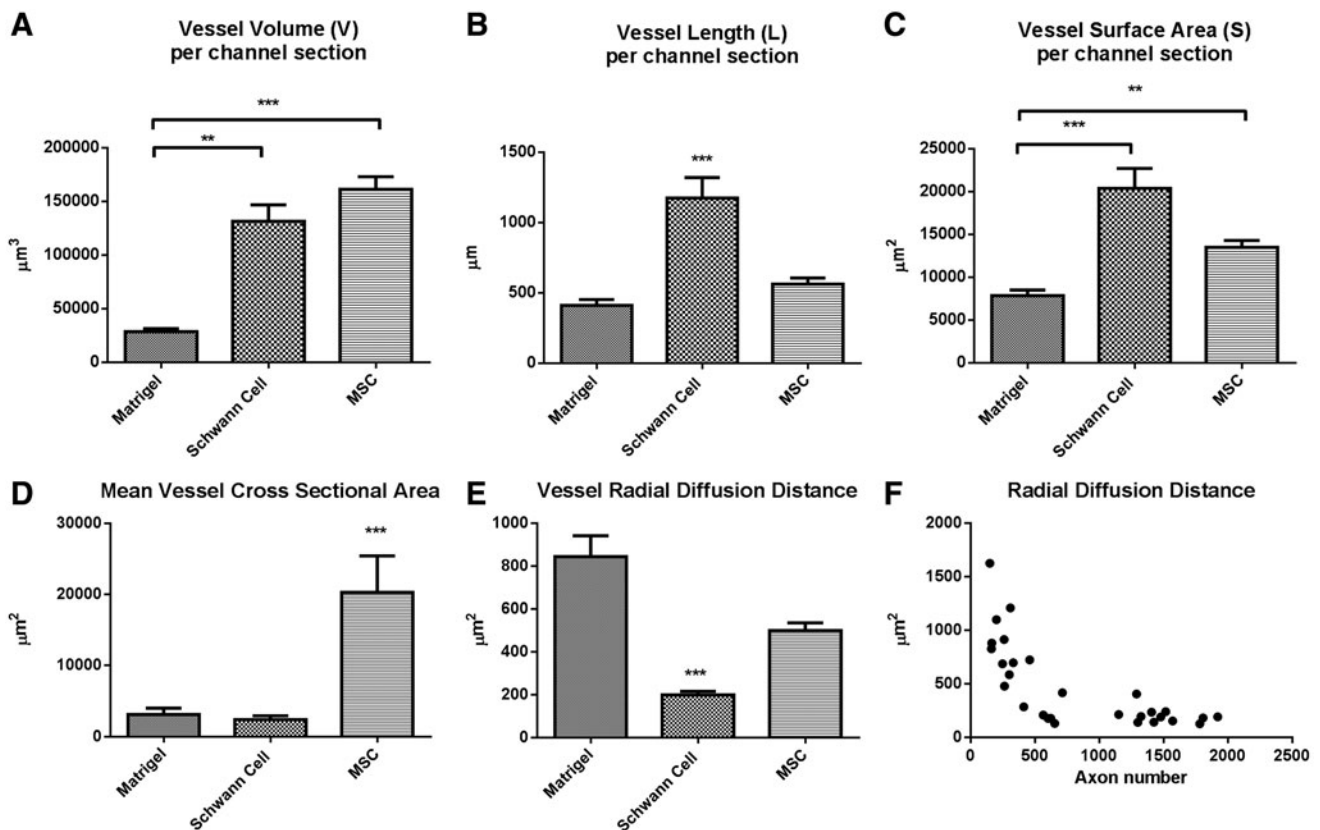

FIG. 5. Unbiased stereology estimates for **(A)** blood vessel volume, **(B)** total blood vessel length, and **(C)** vessel surface area in Matrigel ($n = 93$), Schwann cell ($n = 86$), and eGFP-MSC ($n = 91$) channel sections. Schwann cell channels have a total blood vessel volume and vessel surface area that is comparable to eGFP-MSC channels by virtue of significantly higher vessel length density. **(D)** Mean vessel cross-sectional areas in eGFP-MSC channels exceeded the other animal groups, as calculated from the fractional volume, length, and surface area estimates. **(E)** Estimates for vessel radial diffusion were calculated as inversely proportional to the fractional length volume. **(F)** Total axon number, in Matrigel and Schwann cell groups combined (at $n = 28$ quarter length scaffold intervals), negatively correlated to the mean radial diffusion distance as a hyperbolic function.

Mean vessel diameter was derived from the fractional estimates based upon the ratio of surface to length density. The mean diameter of MSC vessels was $8.11 \pm 0.67 \, \mu m$, of significantly higher caliber than Schwann cell vessels ($4.67 \pm 0.44 \, \mu m$, $p < 0.001$). Mean vessel cross-sectional area (Fig. 5D) in the MSC group also exceeded the other two groups, measuring $20,283 \pm 5141 \, \mu m^2$ compared with the Schwann cell ($2392 \pm 545 \, \mu m^2$) and Matrigel groups ($3120 \pm 883 \, \mu m^2$) ($p < 0.001$). The radial diffusion coefficient is a robust, stereologic measure of a cylindrical zone of diffusion around a blood vessel, calculated as an inverse function of the length density.[49] The diffusion distance for Schwann cell vessels was $198.7 \pm 16.41 \, mm^2$ ($p < 0.001$) compared with $884.0 \pm 97.6 \, mm^2$ in Matrigel channels and $498.8 \pm 35.5 \, mm^2$ (Fig. 5E).

Significant linear correlations were seen between the axon counts and the corresponding vessel length density (Spearman $r = 0.7852$, $p < 0.0001$), vessel surface density (Spearman $r = 0.7719$, $p < 0.0001$), vessel volume fraction (Spearman $r = 0.6862$, $p < 0.0001$), and the mean vessel diameter (Spearman $r = -0.4635$, $p = 0.0113$). There was a statistically significant hyperbolic relationship between axon number and vessel radial diffusion distance (Fig. 5F; Spearman $r = -0.7852$, $p < 0.0001$).

Discussion

OPF$^+$ scaffold channels were seen to be highly cellular, viable environments having separate central core and peripheral compartments. Scaffold channels demonstrated this similarity in their overall architecture regardless of the animal group. Our previous studies have demonstrated that the type of polymer significantly influences the core/peripheral morphology, in that polymers supporting the most clearly demarcated core best supported axonal regeneration.[16] The channel periphery was shown to uniformly stain with antibodies against the astrocyte marker GFAP. As reactive astrocytosis is a primary cellular event in the injury response, migrating astrocytes may preferentially have lined the positively charged channel wall. A significantly higher proportion of channel area was occupied by GFAP-positive cells in the Matrigel group. The result likely reflects the relative availability of space within the Matrigel channel for endogenous cell migration. Sharply demarcated transitions between the astrocyte peripheral zone and central core and were characteristic of the Schwann cell channels in our study. Similar boundaries between astrocytes and transplanted Schwann cells have been observed in other studies, where in vivo[51] and in vitro,[52] Schwann cells are actively excluded from areas occupied by astrocytes.

The molecular components and functional significance of boundary formation in OPF$^+$ scaffold channels is not yet known. In other models, the number of astrocytes expressing chondroitin sulfate proteoglycans is increased in the presence of Schwann cells in coculture.[53] Aggrecan produced by astrocytes inhibited Schwann cell motility on monolayers, while motility could be improved with RNA interference or glycosaminoglycan side chain digestion.[54] Schwann cell conditioned media was sufficient to induce astrocyte hypertrophy, implicating a secreted factor, likely to be a fibroblast-growth factor family member on the basis of FGF ligand and receptor antibody studies.[55] Genetic upregulation of surface integrins could facilitate Schwann cell migration and functional integration into the astrocytic

environment of the injured cord.[56] Regarding function, compartmental boundaries in the CNS including the delineation of segments, developing midlines, tract nuclei, functional columns, and discrete axonal arcs or pathways are demarcated by astrocytes. Increased GFAP staining has been observed in developmental boundaries such as the thalamic nuclei, and barrel cortical structures.[57] The extracellular matrix demarcating these boundaries is laid down by radial astrocytes and is rich in J1/tenascin glycoprotein. Spatial and temporal distributions of tenascin during development also suggest a role in the guidance of neurons within functional patterns.[58] These ''glial cordones'' may be dynamic entities of specialized glia secreting glycoconjugates as mixtures of glycoproteins, glycolipids, and glycosaminoglycans, and which disappear after stable synaptic formation.[59]

Axonal regeneration within the core area of scaffold channels was best supported by Schwann cells, and therefore by means of a hybrid environment of spinal cord and peripheral nervous system cellular elements. Augmentation of the peripheral elements by preloading scaffolds with Schwann cells may improve the efficiency of axonal growth. The result is consistent with our previous observations comparing axonal regeneration in Schwann cell and neural stem cell-loaded scaffold channels.[36] The proportion of channel area occupied by S-100-positive staining at 4 weeks in our current study, however, was not statistically different across the three animals, including the Matrigel only group, which had no transplanted cells. A low proportion of channel area (less than 10%) in our model was occupied by a GFAP$^+$/S-100$^+$ cell type at 4 weeks. Mechanisms to account for cell loss may include cell migration from the scaffold or cell death within the channels. S-100-positive cells seen within the channels may have migrated into the scaffold, as S-100-positive cells were seen in equal proportion across all animal group. These cells stained with both GFAP and S-100, which raises the possibility that they are either an immature astrocyte[60] or an immature Schwann cell[61] phenotype. We have previously shown by electron microscopy that Schwann cells are present and actively myelinate regenerating axons within scaffold channels.[23] Schwann cells migrate in and de-differentiate to an immature phenotype in other complete transection models,[62] regressing from mature P0$^+$ to P0$^-$/p75$^+$ cells that proliferate in the lesion and then gradually re-acquire P0$^+$ maturity.

Peripheral nerve Schwann cells have long been known to freely migrate into the injured cord.[63] Here, they may contribute to endogenous healing by associating with injured axons and remyelinating fibers within the lesion. In contusion injuries, the cystic cavities became partially filled with nerve fibers and associated Schwann cells.[64] Mechanisms accounting the loss of implanted cells may include the robust immune response,[65] poor vascularization and gas exchange,[66] and production of cytotoxic nitrite and lipid free radicals within the anoxic environment.[67] Cell stress given the transition from a nutrient rich culture into the hostile injury environment may also contribute to cell death.[68] That a high proportion of implanted Schwann cells die within the transplant environment has been similarly shown in a contusion model,[69] where the proportion of Schwann cells present within the injury epicenter at 3 weeks posttransplantation fell to $22.4\% \pm 4.3\%$. We would anticipate higher rates of death in

a scaffold model, given that the channel environment would be more anoxic than within the intact, injured cord.

MSCs were seen in implanted OPF[+] scaffolds in equally sparse numbers within the channel core area by eGFP fluorescence at 4 weeks. Pretreatment of scaffolds with eGFP-MSC loading did not support axonal regeneration to any significant extent. This result is not in keeping with the majority of other studies using MSC transplantation techniques in SCI. Since the first described MSC engraftments into the injured cord,[70] some 17 other *in vivo* animal studies have followed.[26] The majority of studies have combined a weight-impactor contusion injury in the rat thoracic followed by direct injection of cultured MSCs into the substance of the cord lesion[70,71] either at the time of the injury of or within 7 days. Cells have also been injected into the rostral and caudal tissue adjacent to the lesion in graded contusion injuries.[72] In one series,[73] cell injection was delayed until 3 months postinjury and the animals were followed out to 1 year.[74] Histologic endpoints have included successful MSC engraftment, remyelination, reduced cavity formation, cell bundle or bridge formation facilitating axonal regeneration, and enhanced Schwann cell migration into the wound. Where functional assessments were done, outcomes included statistical significance of improved BBB scores, increased axonal conduction velocity, improved exploratory rearing behavior, and sensory sensitivity to thermal stimuli.

Few studies however have used polymeric delivery of MSCs. MSCs seeded onto methylacrylate derivatives have been implanted into a cord hemisection model.[75] A reduction in lesion size was noted, along with higher scores in BBB testing and faster recovery of sensitivity in hindlimbs. MSC-seeded scaffolds were also used in bridging a chronic injury, whereby the scaffold was implanted 5 weeks after a balloon compression injury[76] and behavioral testing up to 6 months postimplantation demonstrated functional improvements. The hydrogels were infiltrated with axons, which were myelinated with Schwann cells. Blood vessels and astrocytes also grew inside the implant. MSCs were reported to be present within the hydrogels 5 months after implantation. Our studies[38] are among the few studies that have used a complete transection model for the polymeric delivery of MSCs. Zeng *et al.*[77] have used a collagen-gelatin sponge covered by a thin film of PLGA and seeded with MSCs for implantation into a transection model with primary endpoints of fibronectin deposition and angiogenesis. Our results may demonstrate a necessity for implanted MSCs to integrate with intact nervous tissue in proximity to the injured area.

MSCs in our study were frequently located around the peripheries of blood vessels. That MSCs likely represent subpopulations of pericytes[78,79] is a concept that connects immune and vascular functions implicated in tissue repair via granulation tissue formation.[80] Pericytes from various adult and fetal tissues have also shown expression of classically MSC-type markers, CD44, CD73, CD90, and CD105.[81] Populations of pericytes may in addition have a neuroectodermal origin, derived from Sox1^{+} neuroepithelial/neuro crest cells,[82] an observation that may explain the presence of nerve growth factor receptors on bone marrow MSCs, the potential for MSC neuro-differentiation, and cell tolerance within the CNS environment. Pericytes exist in the brain and retina, at higher densities than in any other organs.[83] Here, the cells may function in the stabilization and maturation of the neurovascular system and the blood–brain barrier. Brain pericytes also have been shown to possess pluripotential activity, and they are recruited at times of ischemic injury.[84] That brain pericytes can contribute to CNS regeneration is in evidence, where the cell type gave rise to neurons and glial cells in the subgranular zone of the dentate gyrus in monkeys following ischemia.[85] Neurogenesis and angiogenesis may be linked through vascular production of stromal-derived factor 1 and angiopoietin 1. These factors can promote neuroblast migration and behavioral recovery[86] in addition to growth and maturation of the vasculature.[87]

MSC channels in our study did not support axonal growth despite appearing to be highly vascular. Matrigel channels minimally supported axonal growth, and were relatively avascular compared with Schwann cell and MSC channels. In Schwann cell channels, high numbers of small diameter vessels were observed, contributing to total vessel lengths of over 1 mm per channel section, twice the total length density seen Matrigel and MSC channels. Schwann cell channel vessels maintained blood volume and surface area estimates to comparable MSC channels, by virtue of high numbers of small vessels. MSC channels maintained their blood supply by means of fewer numbers of vessels of larger caliber. Such observations may further implicate the importance of blood flow rate and the relative success of axonal regeneration, with slow flow predicted through larger diameter vessels formed in MSC channels, and relatively higher flow through higher numbers of tighter vessels in the Schwann cell channel. As such, a significant correlation was shown between decreasing vessel diameter and increasing axon numbers in our study.

Primary fractional estimates of increased length volume, surface density, and volume fraction also significantly correlated to increased axon number. The tightest correlation seen (Spearman $r = 0.7852$, $p < 0.0001$) was between axon number and the length volume. The length volume is of particular physiologic importance as it relates to the radial diffusion distance, the measure of a cylindrical space of tissue around the vessel that will be influenced by diffusion. Of the three channel types, Matrigel demonstrated the highest radial diffusion distances (up to 800 μm) followed by MSC vessels (600 μm). Vessels in Schwann cell channels had distances of around 200 μm. The radial diffusion distances in human spinal cord gray and white matter have been calculated in tissue sections obtained from four cadaver donors.[49] The values were between 15 and 20 μm in both regions, slightly higher in white matter than gray, and importantly were seen to be highly conserved across the four individuals. The coefficient of variance ranged between 3.3% and 5.6%. Conservation of neurovascular parameters in turn applies something of importance for species evolution and survival. Here, we have shown the relationship between radial diffusion distances to mathematically correlate with axon numbers as a hyperbolic function. To achieve physiologic levels axon numbers, there is equal need to improve overall vessel length densities in tissue-engineered spinal cord. Improved axonal growth may depend upon higher numbers of small caliber vessels that provide a close and redundant proximity to the nutrient and oxygen supply.

In conclusion, histologic analysis of the tissue architecture formed after 4 weeks within OPF$^+$ scaffold channels demonstrated established astrocytosis in a circumferential peripheral channel compartment. A structurally separate channel core contained scattered astrocytes, Schwann cells, eGFP-MSCs, blood vessels, and regenerating axons. Axonal counts were augmented by the presence of Schwann cells despite a high proportion of transplanted cell death. MSCs placed in scaffolds also survived at a low rate but did not support axon growth to any extent. The low survival rate of both cell types at 4 weeks contrasts with the dramatic effects on axon number and vessel morphometry. The engrafted cells therefore significantly influenced the microenvironment at an early point and with a longer lasting effect on regeneration. MSCs influenced the formation of vascular elements that were unique. Whereas Schwann cell channels had high numbers of small, densely packed vessels, infrequent and large vessels dominated the structure of MSC scaffold channels. Increased axon counts correlated to higher vessel length and surface density, and with decreasing vessel diameter, implicating the importance of blood flow rate in channels. Radial diffusion distances in vessels significantly correlated to axon number as a hyperbolic function. There is a necessity to engineer higher numbers of small vessels in parallel to improving axonal densities to achieve physiologic relevance and restored neurologic function. Future studies will need to be directed toward understanding early cellular interactions after scaffold implantation and how these may be directed toward increasing vascularity with physiologic characteristics that support regeneration.

Acknowledgments

Disclosure Statement

Senior author has patented with colleagues a spinal cord surgical implant device (US Patent No. 7,163,545).

References

1. Oudega, M., Bradbury, E.J., and Ramer, M.S. Combination therapies. Handb Clin Neurol **109,** 617, 2012.
2. Garcia-Alias, G., Petrosyan, H.A., Schnell, L., Horner, P.J., Bowers, W.J., Mendell, L.M., Fawcett, J.W., and Arvanian, V.L. Chondroitinase ABC combined with neurotrophin NT-3 secretion and NR2D expression promotes axonal plasticity and functional recovery in rats with lateral hemisection of the spinal cord. J Neurosci **31,** 17788, 2011.
3. Kadoya, K., Tsukada, S., Lu, P., Coppola, G., Geschwind, D., Filbin, M.T., Blesch, A., and Tuszynski, M.H. Combined intrinsic and extrinsic neuronal mechanisms facilitate bridging axonal regeneration one year after spinal cord injury. Neuron **64,** 165, 2009.
4. Lu, P., Blesch, A., Graham, L., Wang, Y., Samara, R., Banos, K., Haringer, V., Havton, L., Weishaupt, N., Bennett, D., Fouad, K., and Tuszynski, M.H. Motor axonal regeneration after partial and complete spinal cord transection. J Neurosci **32,** 8208, 2012.
5. Hyatt, A.J., Wang, D., Kwok, J.C., Fawcett, J.W., and Martin, K.R. Controlled release of chondroitinase ABC from fibrin gel reduces the level of inhibitory glycosaminoglycan chains in lesioned spinal cord. J Control Release **147,** 24, 2010.
6. McDonald, J.W., and Sadowsky, C. Spinal-cord injury. Lancet **359,** 417, 2002.
7. Madigan, N.N., McMahon, S., O'Brien, T., Yaszemski, M.J., and Windebank, A.J. Current tissue engineering and novel therapeutic approaches to axonal regeneration following spinal cord injury using polymer scaffolds. Respir Physiol Neurobiol **169,** 183, 2009.
8. Yao, L., Damodaran, G., Nikolskaya, N., Gorman, A.M., Windebank, A., and Pandit, A. The effect of laminin peptide gradient in enzymatically cross-linked collagen scaffolds on neurite growth. J Biomed Mater Res **92A,** 484, 2010.
9. Kang, C.E., Poon, P.C., Tator, C.H., and Shoichet, M.S. A new paradigm for local and sustained release of therapeutic molecules to the injured spinal cord for neuroprotection and tissue repair. Tissue Eng Part A **15,** 595, 2009.
10. Gros, T., Sakamoto, J.S., Blesch, A., Havton, L.A., and Tuszynski, M.H. Regeneration of long-tract axons through sites of spinal cord injury using templated agarose scaffolds. Biomaterials **31,** 6719, 2010.
11. Willerth, S.M., Faxel, T.E., Gottlieb, D.I., and Sakiyama-Elbert, S.E. The effects of soluble growth factors on embryonic stem cell differentiation inside of fibrin scaffolds. Stem Cells **25,** 2235, 2007.
12. Phillips, J.B., King, V.R., Ward, Z., Porter, R.A., Priestley, J.V., and Brown, R.A. Fluid shear in viscous fibronectin gels allows aggregation of fibrous materials for CNS tissue engineering. Biomaterials **25,** 2769, 2004.
13. Nomura, H., Zahir, T., Kim, H., Katayama, Y., Kulbatski, I., Morshead, C.M., Shoichet, M.S., and Tator, C.H. Extramedullary chitosan channels promote survival of transplanted neural stem and progenitor cells and create a tissue bridge after complete spinal cord transection. Tissue Eng Part A **14,** 649, 2008.
14. Dadsetan, M., Szatkowski, J.P., Yaszemski, M.J., and Lu, L. Characterization of photo-cross-linked oligo[poly(ethylene glycol) fumarate] hydrogels for cartilage tissue engineering. Biomacromolecules **8,** 1702, 2007.
15. Tsai, E.C., Dalton, P.D., Shoichet, M.S., and Tator, C.H. Matrix inclusion within synthetic hydrogel guidance channels improves specific supraspinal and local axonal regeneration after complete spinal cord transection. Biomaterials **27,** 519, 2006.
16. Chen, B.K., Knight, A.M., Madigan, N.N., Gross, L., Dadsetan, M., Nesbitt, J.J., Rooney, G.E., Currier, B.L., Yaszemski, M.J., Spinner, R.J., and Windebank, A.J. Comparison of polymer scaffolds in rat spinal cord: a step toward quantitative assessment of combinatorial approaches to spinal cord repair. Biomaterials **32,** 8077, 2011.
17. Dadsetan, M., Knight, A.M., Lu, L., Windebank, A.J., and Yaszemski, M.J. Stimulation of neurite outgrowth using positively charged hydrogels. Biomaterials **30,** 3874, 2009.
18. Franz, S., Weidner, N., and Blesch, A. Gene therapy approaches to enhancing plasticity and regeneration after spinal cord injury. Exp Neurol **235,** 62, 2012.
19. McCall, J., Weidner, N., and Blesch, A. Neurotrophic factors in combinatorial approaches for spinal cord regeneration. Cell Tissue Res **349,** 27, 2012.
20. Jain, A., McKeon, R.J., Brady-Kalnay, S.M., and Bellamkonda, R.V. Sustained delivery of activated Rho GTPases and BDNF promotes axon growth in CSPG-rich regions following spinal cord injury. PLoS One **6,** e16135, 2011.

21. Mehrotra, S., Lynam, D., Liu, C., Shahriari, D., Lee, I., Tuszynski, M., Sakamoto, J., and Chan, C. Time controlled release of arabinofuranosylcytosine (Ara-C) from agarose hydrogels using layer-by-layer assembly: an *in vitro* study. J Biomater Sci Polym Ed **23,** 439, 2012.

22. Oudega, M., Moon, L.D., and de Almeida Leme, R.J. Schwann cells for spinal cord repair. Braz J Med Biol Res **38,** 825, 2005.

23. Chen, B.K., Knight, A.M., de Ruiter, G.C., Spinner, R.J., Yaszemski, M.J., Currier, B.L., and Windebank, A.J. Axon regeneration through scaffold into distal spinal cord after transection. J Neurotrauma **26,** 1759, 2009.

24. Biernaskie, J., Sparling, J.S., Liu, J., Shannon, C.P., Plemel, J.R., Xie, Y., Miller, F.D., and Tetzlaff, W. Skin-derived precursors generate myelinating Schwann cells that promote remyelination and functional recovery after contusion spinal cord injury. J Neurosci **27,** 9545, 2007.

25. Tabesh, H., Amoabediny, G., Nik, N.S., Heydari, M., Yosefifard, M., Siadat, S.O., and Mottaghy, K. The role of biodegradable engineered scaffolds seeded with Schwann cells for spinal cord regeneration. Neurochem Int **54,** 73, 2009.

26. Wright, K.T., El Masri, W., Osman, A., Chowdhury, J., and Johnson, W.E. Concise review: bone marrow for the treatment of spinal cord injury: mechanisms and clinical applications. Stem Cells **29,** 169, 2011.

27. Ritfeld, G.J., Nandoe Tewarie, R.D., Vajn, K., Rahiem, S.T., Hurtado, A., Wendell, D.F., Roos, R.A., and Oudega, M. Bone marrow stromal cell-mediated tissue sparing enhances functional repair after spinal cord contusion in adult rats. Cell Ttransplant **21,** 1561, 2012.

28. Caplan, A.I., and Dennis, J.E. Mesenchymal stem cells as trophic mediators. J Cell Biochem **98,** 1076, 2006.

29. Chopp, M., and Li, Y. Treatment of neural injury with marrow stromal cells. Lancet Neurol **1,** 92, 2002.

30. Li, Y., McIntosh, K., Chen, J., Zhang, C., Gao, Q., Borneman, J., Raginski, K., Mitchell, J., Shen, L., Zhang, J., Lu, D., and Chopp, M. Allogeneic bone marrow stromal cells promote glial-axonal remodeling without immunologic sensitization after stroke in rats. Exp Neurol **198,** 313, 2006.

31. Li, Y., Chen, J., and Chopp, M. Adult bone marrow transplantation after stroke in adult rats. Cell Transplant **10,** 31, 2001.

32. Chen, J., Li, Y., Katakowski, M., Chen, X., Wang, L., Lu, D., Lu, M., Gautam, S.C., and Chopp, M. Intravenous bone marrow stromal cell therapy reduces apoptosis and promotes endogenous cell proliferation after stroke in female rat. J Neurosci Res **73,** 778, 2003.

33. Caplan, A.I. Why are MSCs therapeutic? New data: new insight. J Pathol **217,** 318, 2009.

34. Lu, P., Jones, L.L., and Tuszynski, M.H. BDNF-expressing marrow stromal cells support extensive axonal growth at sites of spinal cord injury. Exp Neurol **191,** 344, 2005.

35. Rooney, G.E., McMahon, S.S., Ritter, T., Garcia, Y., Moran, C., Madigan, N.N., Fluegel, A., Dockery, P., O'Brien, T., Howard, L., Windebank, A.J., and Barry, F. Neurotrophic factor-expressing mesenchymal stem cells survive transplantation into the contused spinal cord without differentiating into neural cells. Tissue Eng Part A **15,** 3049, 2009.

36. Olson, H.E., Rooney, G.E., Gross, L., Nesbitt, J.J., Galvin, K.E., Knight, A., Chen, B., Yaszemski, M.J., and Windebank, A.J. Neural stem cell- and Schwann cell-loaded

biodegradable polymer scaffolds support axonal regeneration in the transected spinal cord. Tissue Eng Part A **15,** 1797, 2009.

37. Krych, A.J., Rooney, G.E., Chen, B., Schermerhorn, T.C., Ameenuddin, S., Gross, L., Moore, M.J., Currier, B.L., Spinner, R.J., Friedman, J.A., Yaszemski, M.J., and Windebank, A.J. Relationship between scaffold channel diameter and number of regenerating axons in the transected rat spinal cord. Acta Biomater **5,** 2551, 2009.

38. Rooney, G.E., Knight, A.M., Madigan, N.N., Gross, L., Chen, B., Giraldo, C.V., Seo, S., Nesbitt, J.J., Dadsetan, M., Yaszemski, M.J., and Windebank, A.J. Sustained delivery of dibutyryl cyclic adenosine monophosphate to the transected spinal cord via oligo [(polyethylene glycol) fumarate] hydrogels. Tissue Eng Part A **17,** 1287, 2011.

39. Rooney, G.E., Moran, C., McMahon, S.S., Ritter, T., Maenz, M., Flugel, A., Dockery, P., O'Brien, T., Howard, L., Windebank, A.J., and Barry, F.P. Gene-modified mesenchymal stem cells express functionally active nerve growth factor on an engineered poly lactic glycolic acid (PLGA) substrate. Tissue Eng Part A **14,** 681, 2008.

40. National Academy of Sciences IfLAR. Guide for the care and use of laboratory animals. In: Earth and Life Sciences NRC, ed. 8th ed. Washington, DC: The National Academies Press, 2010, pp. 1–218.

41. Basso, D.M., Beattie, M.S., and Bresnahan, J.C. A sensitive and reliable locomotor rating scale for open field testing in rats. J Neurotrauma **12,** 1, 1995.

42. Lyck, L., Dalmau, I., Chemnitz, J., Finsen, B., and Schroder, H.D. Immunohistochemical markers for quantitative studies of neurons and glia in human neocortex. J Histochem Cytochem **56,** 201, 2008.

43. Hol, E.M., Roelofs, R.F., Moraal, E., Sonnemans, M.A., Sluijs, J.A., Proper, E.A., de Graan, P.N., Fischer, D.F., and van Leeuwen, F.W. Neuronal expression of GFAP in patients with Alzheimer pathology and identification of novel GFAP splice forms. Mol Psychiatry **8,** 786, 2003.

44. Barnes, C.A., Brison, J., Michel, R., Brown, B.N., Castner, D.G., Badylak, S.F., and Ratner, B.D. The surface molecular functionality of decellularized extracellular matrices. Biomaterials **32,** 137, 2011.

45. Feldman, A.L., Arber, D.A., Pittaluga, S., Martinez, A., Burke, J.S., Raffeld, M., Camos, M., Warnke, R., and Jaffe, E.S. Clonally related follicular lymphomas and histiocytic/dendritic cell sarcomas: evidence for transdifferentiation of the follicular lymphoma clone. Blood **111,** 5433, 2008.

46. Henwood, A.F. The application of heated detergent dewaxing and rehydration to immunohistochemistry. Biotech Histochem **87,** 46, 2010.

47. Howard, C.V., and Reed, M.G. Unbiased Stereology, Three Dimensional Measurement in Microscopy, 2nd ed. Liverpool: QTP Publications, 2010.

48. Garcia, Y., Breen, A., Burugapalli, K., Dockery, P., and Pandit, A. Stereological methods to assess tissue response for tissue-engineered scaffolds. Biomaterials **28,** 175, 2007.

49. Dockery, P., and Fraher, J. The quantification of vascular beds: a stereological approach. Exp Mol Pathol **82,** 110, 2007.

50. Jakubovsky, J., Guller, L., Cerna, M., Balazova, K., Polak, S., Jakubovska, V., and Babal, P. Fluorescence of hematoxylin and eosin-stained histological sections of the human spleen. Acta Histochem **104,** 353, 2002.

51. Baron-Van Evercooren, A., Clerin-Duhamel, E., Lapie, P., Gansmuller, A., Lachapelle, F., and Gumpel, M. The fate of

Schwann cells transplanted in the brain during development. Dev Neurosci **14,** 73, 1992.

52. Afshari, F.T., Kwok, J.C., and Fawcett, J.W. Analysis of Schwann-astrocyte interactions using *in vitro* assays. J Vis Exp **47,** p. doi:pii: 2214, 2011.

53. Lakatos, A., Franklin, R.J., and Barnett, S.C. Olfactory ensheathing cells and Schwann cells differ in their *in vitro* interactions with astrocytes. Glia **32,** 214, 2000.

54. Afshari, F.T., Kwok, J.C., White, L., and Fawcett, J.W. Schwann cell migration is integrin-dependent and inhibited by astrocyte-produced aggrecan. Glia **58,** 857, 2010.

55. Santos-Silva, A., Fairless, R., Frame, M.C., Montague, P., Smith, G.M., Toft, A., Riddell, J.S., and Barnett, S.C. FGF/heparin differentially regulates Schwann cell and olfactory ensheathing cell interactions with astrocytes: a role in astrocytosis. J Neurosci **27,** 7154, 2007.

56. Lavdas, A.A., Papastefanaki, F., Thomaidou, D., and Matsas, R. Cell adhesion molecules in gene and cell therapy approaches for nervous system repair. Curr Gene Ther **11,** 90, 2011.

57. Bushong, E.A., Martone, M.E., and Ellisman, M.H. Examination of the relationship between astrocyte morphology and laminar boundaries in the molecular layer of adult dentate gyrus. J Comp Neurol **462,** 241, 2003.

58. Laywell, E.D., Dorries, U., Bartsch, U., Faissner, A., Schachner, M., and Steindler, D.A. Enhanced expression of the developmentally regulated extracellular matrix molecule tenascin following adult brain injury. Proc Natl Acad Sci U S A **89,** 2634, 1992.

59. Steindler, D.A. Glial boundaries in the developing nervous system. Annu Rev Neurosci **16,** 445, 1993.

60. Chan-Ling, T., Chu, Y., Baxter, L., Weible Ii, M., and Hughes, S. *In vivo* characterization of astrocyte precursor cells (APCs) and astrocytes in developing rat retinae: differentiation, proliferation, and apoptosis. Glia **57,** 39, 2009.

61. Jessen, K.R., and Mirsky, R. The origin and development of glial cells in peripheral nerves. Nat Rev Neurosci **6,** 671, 2005.

62. Nagoshi, N., Shibata, S., Hamanoue, M., Mabuchi, Y., Matsuzaki, Y., Toyama, Y., Nakamura, M., and Okano, H. Schwann cell plasticity after spinal cord injury shown by neural crest lineage tracing. Glia **59,** 771, 2011.

63. Feigin, I., and Ogata, J. Schwann cells and peripheral myelin within human central nervous tissues: the mesenchymal character of Schwann cells. J Neuropathol Exp Neurol **30,** 603, 1971.

64. Beattie, M.S., Bresnahan, J.C., Komon, J., Tovar, C.A., Van Meter, M., Anderson, D.K., Faden, A.I., Hsu, C.Y., Noble, L.J., Salzman, S., and Young, W. Endogenous repair after spinal cord contusion injuries in the rat. Exp Neurol **148,** 453, 1997.

65. Laylor, R., Dewchand, H., Simpson, E., and Dazzi, F. Engraftment of allogeneic hematopoietic stem cells requires both inhibition of host-versus-graft responses and 'space' for homeostatic expansion. Transplantation **79,** 1484, 2005.

66. Griffiths, I.R. Spinal cord blood flow after acute experimental cord injury in dogs. J Neurol Sci **27,** 247, 1976.

67. Braughler, J.M., and Hall, E.D. Involvement of lipid peroxidation in CNS injury. J Neurotrauma **9 Suppl 1,** S1, 1992.

68. Brundin, P., Karlsson, J., Emgard, M., Schierle, G.S., Hansson, O., Petersen, A., and Castilho, R.F. Improving the survival of grafted dopaminergic neurons: a review over current approaches. Cell Transplant **9,** 179, 2000.

69. Pearse, D.D., Sanchez, A.R., Pereira, F.C., Andrade, C.M., Puzis, R., Pressman, Y., Golden, K., Kitay, B.M., Blits, B., Wood, P.M., and Bunge, M.B. Transplantation of Schwann cells and/or olfactory ensheathing glia into the contused spinal cord: Survival, migration, axon association, and functional recovery. Glia **55,** 976, 2007.

70. Chopp, M., Zhang, X.H., Li, Y., Wang, L., Chen, J., Lu, D., Lu, M., and Rosenblum, M. Spinal cord injury in rat: treatment with bone marrow stromal cell transplantation. Neuroreport **11,** 3001, 2000.

71. Ankeny, D.P., McTigue, D.M., and Jakeman, L.B. Bone marrow transplants provide tissue protection and directional guidance for axons after contusive spinal cord injury in rats. Exp Neurol **190,** 17, 2004.

72. Himes, B.T., Neuhuber, B., Coleman, C., Kushner, R., Swanger, S.A., Kopen, G.C., Wagner, J., Shumsky, J.S., and Fischer, I. Recovery of function following grafting of human bone marrow-derived stromal cells into the injured spinal cord. Neurorehabil Neural Repair **20,** 278, 2006.

73. Vaquero, J., Zurita, M., Oya, S., and Santos, M. Cell therapy using bone marrow stromal cells in chronic paraplegic rats: systemic or local administration? Neurosci Lett **398,** 129, 2006.

74. Zurita, M., and Vaquero, J. Bone marrow stromal cells can achieve cure of chronic paraplegic rats: functional and morphological outcome one year after transplantation. Neurosci Lett **402,** 51, 2006.

75. Sykova, E., Jendelova, P., Urdzikova, L., Lesny, P., and Hejcl, A. Bone marrow stem cells and polymer hydrogels—two strategies for spinal cord injury repair. Cell Mol Neurobiol **26,** 1113, 2006.

76. Hejcl, A., Sedy, J., Kapcalova, M., Toro, D.A., Amemori, T., Lesny, P., Likavcanova-Masinova, K., Krumbholcova, E., Pradny, M., Michalek, J., Burian, M., Hajek, M., Jendelova, P., and Sykova, E. HPMA-RGD hydrogels seeded with mesenchymal stem cells improve functional outcome in chronic spinal cord injury. Stem Cells Dev **19,** 1535, 2010.

77. Zeng, X., Zeng, Y.S., Ma, Y.H., Lu, L.Y., Du, B.L., Zhang, W., Li, Y., and Chan, W.Y. Bone marrow mesenchymal stem cells in a three-dimensional gelatin sponge scaffold attenuate inflammation, promote angiogenesis, and reduce cavity formation in experimental spinal cord injury. Cell Transplant **20,** 1881, 2011.

78. Crisan, M., Deasy, B., Gavina, M., Zheng, B., Huard, J., Lazzari, L., and Peault, B. Purification and long-term culture of multipotent progenitor cells affiliated with the walls of human blood vessels: myoendothelial cells and pericytes. Methods Cell Biol **86,** 295, 2008.

79. Caplan, A.I. All MSCs are pericytes? Cell Stem Cell **3,** 229, 2008.

80. da Silva Meirelles, L., Caplan, A.I., and Nardi, N.B. In search of the *in vivo* identity of mesenchymal stem cells. Stem Cells **26,** 2287, 2008.

81. Augello, A., Kurth, T.B., and De Bari, C. Mesenchymal stem cells: a perspective from *in vitro* cultures to *in vivo* migration and niches. Eur Cell Mater **20,** 121, 2010.

82. Takashima, Y., Era, T., Nakao, K., Kondo, S., Kasuga, M., Smith, A.G., and Nishikawa, S. Neuroepithelial cells supply an initial transient wave of MSC differentiation. Cell **129,** 1377, 2007.

83. Shepro, D., and Morel, N.M. Pericyte physiology. FASEB J **7,** 1031, 1993.

84. Kamouchi, M., Ago, T., Kuroda, J., and Kitazono, T. The possible roles of brain pericytes in brain ischemia and stroke. Cell Mol Neurobiol **32,** 159, 2012.

85. Yamashima, T., Tonchev, A.B., Vachkov, I.H., Popivanova, B.K., Seki, T., Sawamoto, K., and Okano, H. Vascular adventitia generates neuronal progenitors in the monkey hippocampus after ischemia. Hippocampus **14,** 861, 2004.

86. Ohab, J.J., Fleming, S., Blesch, A., and Carmichael, S.T. A neurovascular niche for neurogenesis after stroke. J Neurosci **26,** 13007, 2006.

87. Oudega, M. Molecular and cellular mechanisms underlying the role of blood vessels in spinal cord injury and repair. Cell Tissue Res **349,** 269, 2012.

Address correspondence to:
Anthony J. Windebank, MD
Department of Neurology
Mayo Clinic College of Medicine
Mayo Clinic
200 First St. SW
Rochester, MN 55905

E-mail: windebank.anthony@mayo.edu